PHYSICAL REVIEW B **72**, 075132 (2005)

Role of Er^{3+} concentration in high-resolution spectra of BaY_2F_8 single crystals

A. Baraldi, R. Capelletti,* M. Mazzera, A. Ponzoni, G. Amoretti, and N. Magnani
Istituto Nazionale per la Fisica della Materia (INFM-CNR), Physics Department, University of Parma,
Parco Area delle Scienze 7/A, 43100 Parma, Italy

A. Toncelli and M. Tonelli
Istituto Nazionale per la Fisica della Materia (INFM-CNR), NEST, Physics Department, University of Pisa,
Via F. Buonarroti 2, 56127 Pisa, Italy

(Received 23 December 2004; published 23 August 2005)

Fourier transform absorption spectroscopy with a resolution as fine as 0.02 cm^{-1} was applied to Er^{3+}-doped monoclinic BaY_2F_8 laser crystals in a wide wave number range ($500-24\,000$ cm^{-1}) and in the temperature range 9–300 K. The careful analysis of the complex narrow line spectra induced by Er^{3+} allowed us to determine with high accuracy the crystal field splitting of the fundamental $^4I_{15/2}$ and of the excited $^4I_{13/2}$, $^4I_{11/2}$, $^4I_{9/2}$, $^4F_{9/2}$, $^4S_{3/2}$, $^2H_{11/2}$, $^4F_{7/2}$, $^4F_{5/2}$, and $^4F_{3/2}$ manifolds. On the basis of the experimental data, the crystal-field parameters were determined and Newman's superposition model was applied: in this way a slight displacement of Er^{3+} with respect to the Y^{3+} position was foreseen. The Judd-Ofelt parameters were evaluated: the lifetime values deduced from them were compared to the experimental ones and discussed. The effects caused by increasing Er^{3+} concentrations (0.5%, 2%, 12%, and 20% atomic fraction) were studied in detail. The new lines, the line broadening, and the line-shape changes were explained in terms of Er^{3+}-Er^{3+} interaction.

DOI: 10.1103/PhysRevB.72.075132 PACS number(s): 78.30.Am, 71.55.−i, 71.70.−d

I. INTRODUCTION

Yttrium fluoride single crystals doped with trivalent rare-earth (RE^{3+}) ions are good candidates as active materials for new generation lasers in the $2-4$ μm range; the rather low phonon energies ($h\nu_{max} \sim 450$ cm^{-1}),[1] e.g., lower than those of the more widely used YAG, suggest a reduced weight of the nonradiative processes with respect to the radiative emission.[2] For example, erbium-doped BaY_2F_8 single crystals supply an efficient laser emission at 2.8 μm, which can be absorbed by the OH groups present in the living tissues and therefore exploited for medical applications.[3] The BaY_2F_8 crystal structure is monoclinic (space group $C2/m$) with lattice parameters as follows: $a=6.9829$ Å, $b=10.519$ Å, $c=4.2644$ Å, $\alpha=\beta=90°$, and $\gamma=99.676°$.[4,5] Each unit cell contains two formula units. ESR measurements have proven that RE^{3+} enters the BaY_2F_8 lattice by occupying the Y^{3+} site,[6] which has C_2 symmetry, and is surrounded by eight F^- ions.[4] Since the RE^{3+} substitutes for the homovalent Y^{3+}, the charge compensation is not required, therefore high RE^{3+} solubility is expected, which could be exploited to enhance the laser emission output.[3] However, by increasing the RE^{3+} concentration, the average distance between two RE^{3+} ions decreases and, at high RE^{3+} concentrations, more or less loose RE^{3+} pairs might be formed: in this case a stronger interaction is expected. Impurity clustering is a well-known phenomenon, widely investigated by means of a number of dielectric and optical techniques, in model systems such as alkali halides and alkali earth fluorides doped with aliovalent cations.[7] In the former case the cation vacancy (V), charge compensating a divalent cation impurity (I), provides mobility to the so-formed defect (IV dipole), which migrates in the lattice until encountering another (or other) dipole(s). In this way clusters and complexes (e.g., dimers, trimers) are originated, which at ordinary temperatures are more stable than the isolated dipoles,[7,8] e.g., the solubility limit of dispersed IV dipoles was found as low as a few parts per million (p.p.m.) at room temperature (RT). In alkali earth fluorides (e.g., CaF_2 and SrF_2) the RE^{3+} ion enters substituting for divalent alkali earth and is charge compensated by a mobile interstitial F^-: a variety of RE^{3+} cluster configurations were reported.[7,8] The presence of Er^{3+} clusters was detected and analyzed in CaF_2 by means of selective laser excitation[9] and more recently in $LiNbO_3$ by means of combined excitation-emission spectroscopy.[10] In the case of yttrium fluorides, such as the most extensively investigated BaY_2F_8 and $LiYF_4$, no direct evidence of RE^{3+} clusters has been reported. However, dopant concentration effects on the optical performances of the lasing crystals were monitored and considered. For example, by increasing the RE^{3+} concentration the initial increase of the slope efficiency of the $2.8-3$ μm laser emission in BaY_2F_8:Er^{3+} is followed by a decrease[3,11] and the lifetime of different excited levels in $LiYF_4$ and BaY_2F_8 shortens, due to a strong short-range interaction and energy transfer between neighbor RE^{3+} ions.[12,13] Hints about clustering phenomena can be found in the superlinear dependence of some vacuum ultraviolet RE^{3+} absorption band amplitude on the dopant concentration and in the segregation of Nd^{3+}, Er^{3+}, and Ho^{3+} in BaY_2F_8.[14]

The Er^{3+} electronic transitions, exploited for laser emission, occur within the shielded $4f$ shell. More specifically, in the case of BaY_2F_8 the RE^{3+} substituting for the Y^{3+} is surrounded by an eight F^- polyhedron which provides a further shield.[4] Therefore, the spectroscopic identification of different RE^{3+} environments originated by increasing the dopant concentration might look like a rather difficult task. However, due to the weak coupling of the optical f electron to the surrounding, the absorption lines are, as a rule, very narrow at low temperatures. For example, extremely narrow linewidths of 40–160 MHz (10^{-3}–4×10^{-3} cm^{-1}) were observed for the $^4I_{15/2}\rightarrow{}^4F_{9/2}$ transition (at 15 302.4 cm^{-1}) in a low-strain, isotopically pure (99.9% ^{7}Li) $LiYF_4$ crystal containing naturally occurring levels of Er^{3+} impurities (~1 p.p.m.).[15]

In the present work spectra of BaY_2F_8 single crystals, doped with Er^{3+} atomic fraction (F_{Er}^{at}) in the range 0.5% to 20%, are investigated. Therefore, also on the basis of preliminary measurements,[16] a line broadening, due either to the natural isotopic distribution of Ba, Y, and Er or to the increasing concentration of the last should be considered. However, for most of the Er^{3+} lines, the linewidth at low temperature remains below 1 cm^{-1}, therefore high-resolution optical spectroscopy can be successfully exploited to discriminate between different Er^{3+} environments.[16] Because of the electrostatic and spin-orbit interaction, the $4f^{11}$ configuration of the free Er^{3+} ion is split into 41 manifolds, the further splitting of them being caused by the crystal field when the ion is embedded into a crystal lattice.[17] In the case of BaY_2F_8 the energies of the RE^{3+} transitions among a few different manifolds, particularly those exploited for lasing and for up-conversion experiments, are known, mainly from fluorescence measurements performed at 77 and/or 300 K with a wave number accuracy in the range 0.5–2 cm^{-1}.[1,5,13,18,19]

High-resolution (0.02 cm^{-1}) Fourier transform absorption spectroscopy is applied in the present work to Er^{3+}-doped BaY_2F_8 single crystals in a wide wave-number range (500–24 000 cm^{-1}) and in the temperature range 9–300 K to get a complete and detailed analysis of the complex narrow line spectra, induced by Er^{3+}. The aims are (1) to determine with high accuracy the crystal field splitting of the fundamental $^4I_{15/2}$ and of the excited $^4I_{13/2}$, $^4I_{11/2}$, $^4I_{9/2}$, $^4F_{9/2}$, $^4S_{3/2}$, $^2H_{11/2}$, $^4F_{7/2}$, $^4F_{5/2}$, and $^4F_{3/2}$ states, (2) to evaluate the Judd-Ofelt[20–22] parameters, and (3) to analyze the role played by the Er^{3+} concentration on the spectra. The experimental values of the energy levels are fitted in the framework of the single-ion model. The so-obtained crystal field parameters are then compared to those calculated by using Newman's superposition model,[23] thus gaining information on the local structural modifications which occur when a Y^{3+} ion is substituted by Er^{3+}. From the Judd-Ofelt parameters, derived from the absorption spectra, the radiative lifetimes of different excited states are evaluated, compared to those measured on the same sample from the light emission decay, and also discussed in the framework of other results quoted in the literature. By increasing F_{Er}^{at} from 0.5% to 20%, new features are displayed by the spectra, as an inhomogeneous line broadening and new absorption lines. The former effect is attributed to the random distribution of the Er^{3+} ions on the Y^{3+} sites, which slightly modifies the crystal field probed by a given Er^{3+} and the latter to the formation of more or less loose Er^{3+}-Er^{3+} pairs. Each of them exhibits its own distinct level scheme, which is discussed in terms of meaningful crystal field modifications, with respect to that experienced by the isolated Er^{3+}.

II. EXPERIMENTAL DETAILS

The BaY_2F_8 single crystals were grown by a computer-controlled Czochralski technique under a purified argon atmosphere.[24] The samples were prepared from 5N pure BaF_2, YF_3, and ErF_3 supplied by AC Materials. Crystals with different Er^{3+} concentrations were investigated. The Er^{3+} doping level is given in terms of atomic fraction F_{Er}^{at}, i.e., the ratio between the numbers of Er^{3+} and Y^{3+} ions. The Er^{3+} concentration N_{Er}, i.e., the number of Er^{3+} ions per unit volume, can be evaluated from F_{Er}^{at} and Y^{3+} concentration, which is 1.283×10^{22} cm^{-3}.[5] Four values of F_{Er}^{at} were chosen, i.e., 0.5%, 2%, 12%, and 20%. All the F_{Er}^{at} values are related to the atomic fraction added to the melt. No direct measurement of the actual F_{Er}^{at} in the crystals was performed. Nevertheless the Er^{3+} distribution coefficient is generally assumed equal to one if Er^{3+} substitutes for Y^{3+}, as in the present case, due to the comparable ionic radii of the two ions. Therefore the F_{Er}^{at} in the melt can be taken as a good approximation of the one in the crystal. Nominally pure samples were also analyzed as references. The samples were oriented, cut, and polished. The sample thickness ranged between 0.9 and 7.5 mm. As BaY_2F_8 is a biaxial crystal, the three perpendicular direction method (TPM)[25] was applied to evaluate the Judd-Ofelt parameter (Sec. IV B). Therefore a parallelepiped of $3.6\times4.8\times5.7$ mm^3 was cut from a $BaY_2F_8:Er^{3+}$ 2 at. % crystal: the six surfaces were polished to allow the measurements of the spectra along three orthogonal directions.

The optical absorption spectra were monitored by means of a Fourier transform (FT) spectrometer Bomem DA8 operating in the 500–24 000 cm^{-1} range with an apodized resolution as fine as 0.02 cm^{-1}. In the following the absorption lines are labeled by their position (wave number) as measured at 9 K, unless otherwise stated. As the infrared detectors employed are affected by nonlinear behavior when large variations of photon fluxes are involved, i.e., in the case of absorption measurements for high absorbance values, the quantitative considerations on the absorption line amplitudes were restricted to lines with peak absorbance lower than one. The sample temperature was controlled in the 9–300 K range by means of a 21SC model Cryodine Cryocooler of CTI Cryogenics equipped with KRS5 and fused silica windows.

The visible and infrared emission decay times were measured by exciting the sample using both the fundamental and the frequency-doubled emission of a pulsed tunable $Ti:Al_2O_3$ laser. The emitted light was focused by a lens on the input slit of a monochromator having 0.25 m focal length and detected by a suitable detector (photomultiplier, or InSb). The signal from the detector was sent to a digital oscilloscope. The shortest response time of the system was about 1 μs.

Weak traces of other RE^{3+}, like Nd^{3+}, Ho^{3+}, Dy^{3+}, and Tm^{3+}, could be detected in the samples, thanks to the high-resolution spectroscopy applied at 9 K. Each impurity was identified by comparing the position of the very weak lines, detected in the spectra, either with those of available samples intentionally doped with a given RE^{3+} or with the data quoted in the literature.[22,26] For example, the unwanted Er^{3+} concentration in a nominally pure sample was roughly estimated as low as 50 p.p.m. (see Sec. IV D 1). No trace of

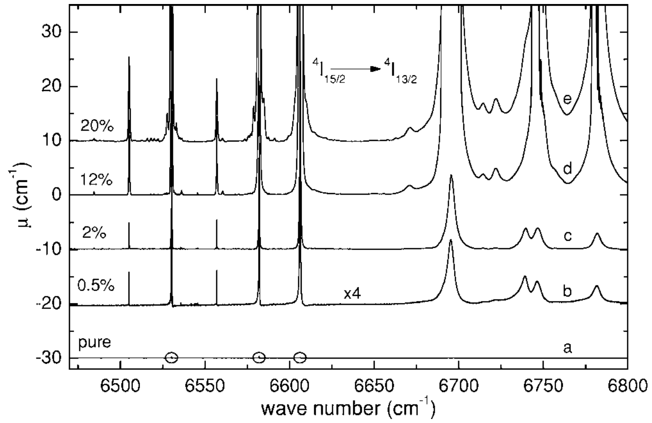

FIG. 1. Optical absorption spectra measured at 9 K in the region of the $^4I_{15/2} \rightarrow {}^4I_{13/2}$ Er^{3+} transition for BaY_2F_8 samples doped with different $F_{\rm Er}^{\rm at}$ and for a pure sample. Curve *a*—pure sample, res. $=0.1$ cm^{-1}; curve b—$F_{\rm Er}^{\rm at}=0.5\%$, res. $=0.02$ cm^{-1}; curve *c*—$F_{\rm Er}^{\rm at}=2\%$, res. $=0.04$ cm^{-1}; curve *d*—$F_{\rm Er}^{\rm at}=12\%$, res. $=0.04$ cm^{-1}; and curve *e*—$F_{\rm Er}^{\rm at}=20\%$, res. $=0.4$ cm^{-1}.

OH^- ions was detected, at least in samples as thick as 7.5 mm and within the sensitivity limits of the present experimental setup, which was proven to monitor hydroxyl ion doping levels as low as 3×10^{12} cm^{-3} in one thick (4 cm) LiF: Mg (Ref. 27) and ~0.2 p.p.m. in a 1 mm thick $KMgF_3$.[28] The result emphasizes the laser quality of the samples grown and investigated in the present work, since OH-containing species are known to cause luminescence quenching.[29–31]

Preliminary linear dichroism measurements were performed in the infrared by using a gold grid polarizer deposited onto a KRS5 substrate.

X-ray diffraction measurements, performed at INTIBS (Wrocław, Poland) with a single crystal diffractometer KM-4 by KUMA Diffraction equipped with x-ray CCD detector, showed that no phase separation occurs even in highly doped samples (Er^{3+} 20 at. %).

For thermal treatments a thin sample was kept in a fused silica tube for 4 h at 600 °C, then cooled to room temperature onto a copper plate.

III. RESULTS

A. Effects of the Er^{3+} concentration on the 9 K spectra

The complex narrow line absorption spectra, related to the Er^{3+} transitions from the fundamental $^4I_{15/2}$ to the excited $^4I_{13/2}$, $^4I_{11/2}$, $^4I_{9/2}$, $^4F_{9/2}$, $^4S_{3/2}$, $^2H_{11/2}$, $^4F_{7/2}$, $^4F_{5/2}$, and $^4F_{3/2}$ manifolds, were monitored at 9 K by applying the high-resolution spectroscopy to BaY_2F_8 samples doped with the four $F_{\rm Er}^{\rm at}$ quoted in Sec. II. Examples of such spectra, measured at 9 K, are provided by Figs. 1 and 2 for the $^4I_{15/2} \rightarrow {}^4I_{13/2}$ and $^4I_{15/2} \rightarrow {}^4I_{11/2}$ transitions, respectively. For the sake of comparison the spectrum of a nominally pure BaY_2F_8 sample is displayed in Fig. 1, curve *a*. The line amplitudes increase by increasing the Er^{3+} concentration: this is clearly proven in Fig. 1 by the medium intensity lines, as for example the lines at 6505.15, 6556.99, and 6695.60 cm^{-1}, respectively. The spectrum of the nominally pure sample is practically flat: only three extremely weak lines are detected at 6530.23, 6582.44, and 6606.23 cm^{-1}, respectively, exactly in correspondence of the strongest lines observed in Er^{3+}-doped samples (in Fig. 1 they are marked with circles).

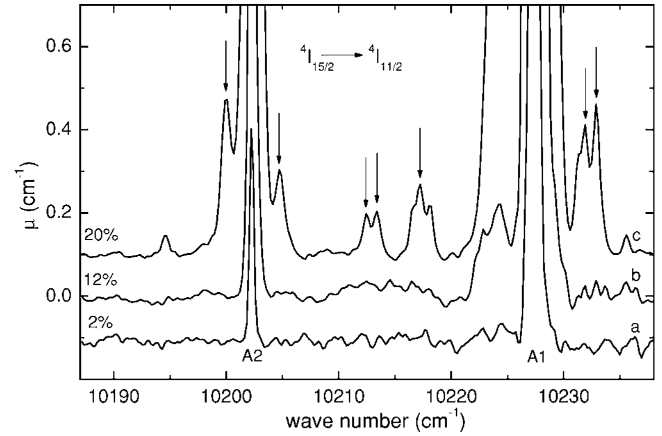

FIG. 2. Optical absorption spectra measured at 9 K in the region of the $^4I_{15/2} \rightarrow {}^4I_{11/2}$ Er^{3+} transition for BaY_2F_8 samples doped with different $F_{\rm Er}^{\rm at}$. Curve *a*—$F_{\rm Er}^{\rm at}=2\%$, res. $=0.4$ cm^{-1}; curve *b*—$F_{\rm Er}^{\rm at}=12\%$, res. $=0.4$ cm^{-1}; and curve *c*—$F_{\rm Er}^{\rm at}=20\%$, res. $=0.4$ cm^{-1}.

The linewidths increase by increasing the doping level, as displayed in Fig. 3 for the weak 6484.36 cm^{-1} line, while the positions are independent of the Er^{3+}-concentration, as clearly shown in Figs. 1–4. In Fig. 3 the lines, normalized to their maximum amplitude, are portrayed for different $F_{\rm Er}^{\rm at}$, e.g., for 2 (curve *a*), 12 (curve *b*), and 20 Er^{3+} at. % (curve *c*), respectively. In samples with the lowest Er^{3+} doping (0.5 at. %) the linewidth is as small as 0.13 cm^{-1}. It should be remarked that, for a given $F_{\rm Er}^{\rm at}$, the lines occurring at the lowest wave numbers are the narrowest (see for example Fig. 1, where the lines below 6620 cm^{-1} are significantly nar-

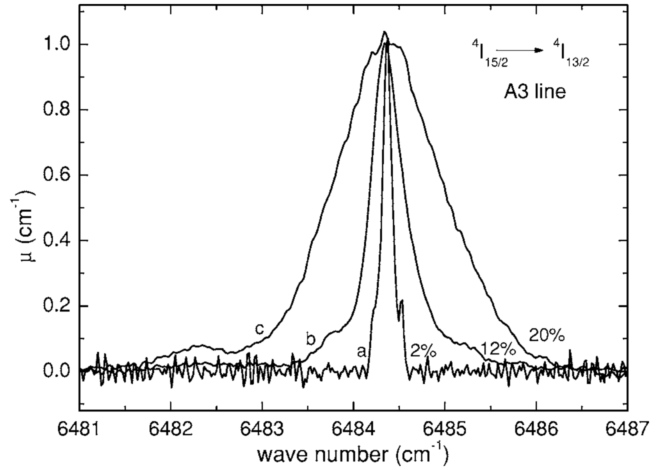

FIG. 3. Optical absorption spectra measured at 9 K and related to the A3 line at 6484.36 cm^{-1} within the $^4I_{15/2} \rightarrow {}^4I_{13/2}$ Er^{3+} transition for BaY_2F_8 samples doped with different $F_{\rm Er}^{\rm at}$. The peak amplitudes are normalized to one. Curve *a*—$F_{\rm Er}^{\rm at}=2\%$, res. $=0.04$ cm^{-1}; curve *b*—$F_{\rm Er}^{\rm at}=12\%$, res. $=0.04$ cm^{-1}; and curve *c*—$F_{\rm Er}^{\rm at}=20\%$, res. $=0.04$ cm^{-1}.

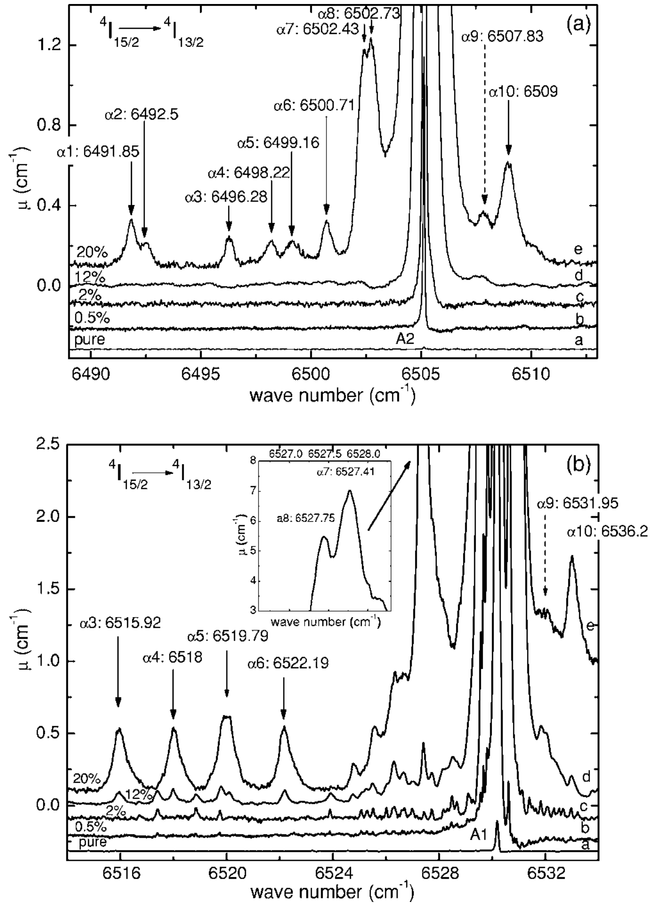

FIG. 4. Magnification of the optical absorption spectra measured at 9 K in the region of the $^4I_{15/2} \rightarrow {}^4I_{13/2}$ Er^{3+} transition for BaY_2F_8 samples doped with different F_{Er}^{at} and for a pure sample. The purpose is to put in evidence the weaker lines. Panels (a) and (b) display the regions around the A2 line at 6505.15 cm^{-1} and the A1 line at 6530.23 cm^{-1}, respectively. The inset in panel (b) gives further details of the spectra, as obtained from a thinner sample (thickness=0.9 mm). In all panels: curve *a*—pure sample, res. =0.1 cm^{-1}; curve *b*—F_{Er}^{at}=0.5%, res. =0.02 cm^{-1}; curve *c*—F_{Er}^{at} =2%, res. =0.04 cm^{-1}; curve *d*—F_{Er}^{at}=12%, res. =0.04 cm^{-1}; and curve *e*—F_{Er}^{at}=20%, res. =0.04 cm^{-1}.

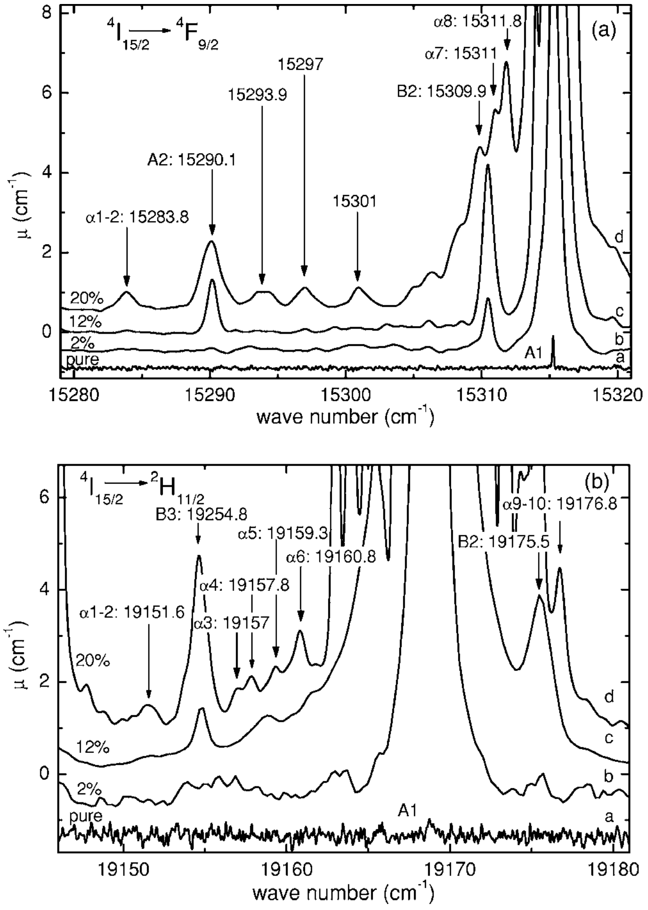

FIG. 5. Magnification of the optical absorption spectra measured at 9 K for BaY_2F_8 samples doped with different F_{Er}^{at} and for a pure sample. The purpose is to put in evidence the weaker lines. Panels (a) and (b) display the regions around the A1 lines at 15 315.20 cm^{-1} and at 19 168.72 cm^{-1}, within the $^4I_{15/2} \rightarrow {}^4F_{9/2}$ and $^4I_{15/2} \rightarrow {}^2H_{11/2}$ Er^{3+} transitions, respectively. In all panels: curve *a*—pure sample, res. =0.1 cm^{-1}; curve *b*—F_{Er}^{at}=2%, res. =0.5 cm^{-1}; curve *c*—F_{Er}^{at}=12%, res. =0.5 cm^{-1}; and curve *d*—F_{Er}^{at}=20%, res. =0.5 cm^{-1}.

rower than those appearing above 6650 cm^{-1}, see Sec. IV D 2).

Additional weaker peaks are detected in the most heavily doped samples; compare, for example, curves *e* and *d* with curve *b* in Fig. 1 in the wave number region 6507–6530 cm^{-1}. The additional peaks, indicated by arrows, in the region of the $^4I_{15/2} \rightarrow {}^4I_{13/2}$ transition can be more easily distinguished by inspecting the magnified spectra displayed by Figs. 4(a) (6489–6513 cm^{-1} region) and 4(b) (6514–6534 cm^{-1} region). Additional lines are also observed in other spectral ranges where the Er^{3+} optical absorption transitions occur: examples of them, indicated by arrows, are portrayed in Figs. 2 ($^4I_{15/2} \rightarrow {}^4I_{11/2}$ transition), Fig. 5(a) ($^4I_{15/2} \rightarrow {}^4F_{9/2}$ transition), and Fig. 5(b) ($^4I_{15/2} \rightarrow {}^2H_{11/2}$ transition).

As mentioned above, in the spectra of a nominally pure sample very weak lines appear exactly at the same wave numbers as a few strong lines in Er^{3+}-doped samples: examples are those peaking at 6505.15, 6530.23, 6582.44, 6606.23, and 15315.20 cm^{-1} [see Figs. 1, 4(a), 4(b), and 5(a)]. This result suggests that weak unwanted traces of Er^{3+} are present even in the nominally pure sample and can be detected due to the sensitivity of the high resolution FT spectroscopy applied at low temperature.

The analysis and the origin of the lines are discussed in Secs. IV A and IV D 3.

B. Effects of temperature on the spectra

By increasing the temperature the lines broaden and shift. The amplitude decreases for some of them, while it increases for others. Sharp, well-resolved lines, especially in the 6450–6650 cm^{-1} region, are observed at 9 K. The lines are broader at 80 K and new ones appear with respect to those measured at 9 K: they are characterized by a marked overlapping. At 300 K a broad, weak, practically structureless spectrum is detected. Details for a few lines, which work as examples, are shown by Fig. 6. By increasing the temperature, the line peaking at 6606.23 cm^{-1} broadens, becomes weaker and weaker, and shifts towards lower wave numbers [Fig. 6(a)]. On the contrary, the line at 6505.15 cm^{-1} is strongly enhanced at 30 K, then decreases, broadens, and shifts towards higher wave numbers [Fig. 6(b)]. Figure 7 summarizes the behavior of three lines (at 6530.23, 6505.15, and 6484.36 cm^{-1}) for what concerns the peak absorption coefficient μ vs. temperature [Figs. 7(a)–7(c), respectively]. However, it should be remarked that the line amplitude decrease, displayed in Figs. 7(a)–7(c), is emphasized by the simultaneous temperature induced line broadening [see, for example, Fig. 6(b) for the 6505.15 cm^{-1} line]. The width change is taken into account by Fig. 7(d), which portrays the behavior of the area $\mathcal{A}$, subtended to the absorption line, versus the temperature for the 6505.15, 6484.36, and 6428.60 cm^{-1} lines. Their area increases monotonically with the temperature and does not show any maximum, as, on the contrary, displayed by the absorption coefficient in Fig. 7(b) and 7(c). At variance with respect to the other lines, the area under the 6530.23 cm^{-1} line [not displayed in Fig.7(d) for the sake of clarity] decreases monotonically, as the absorption coefficient does [Fig. 7(a)].

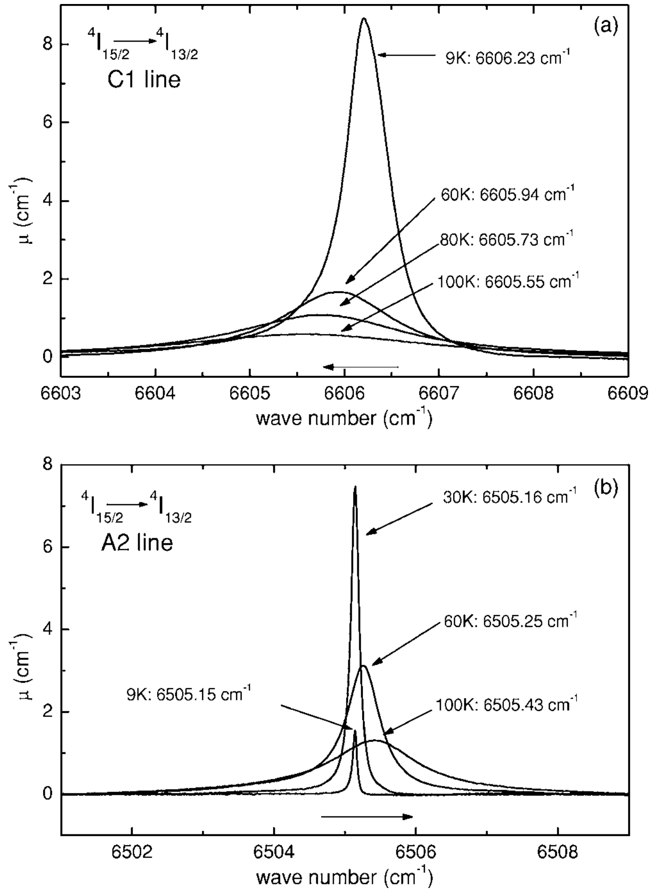

FIG. 6. Temperature dependence of the optical absorption spectra in the region of $^4I_{15/2} \rightarrow {^4I_{13/2}}$ Er^{3+} transition for a BaY_2F_8:Er^{3+} 0.5 at. %. Panels (a) and (b) display the detailed temperature dependence of two lines, i.e., the C1 line at 6606.23 cm^{-1} and the A2 line at 6505.15 cm^{-1}, respectively. The measurement temperatures and the related peak positions are indicated by arrows. The resolution is 0.02 cm^{-1} for the spectra measured at 9 K and 0.04 for the other temperatures.

C. Anisotropy of the spectra

BaY_2F_8 is a low symmetry crystal (see Sec. I): it is monoclinic and biaxial. Therefore, the Er^{3+} impurity absorption line amplitudes might change by changing the direction of the incident light beam and/or its polarization. Preliminary measurements performed by using linearly polarized light showed that the Er^{3+} spectra are dichroic. An example is given by Fig. 8(a), where spectra of a BaY_2F_8:Er^{3+} 20 at. % sample are compared for two different light polarization directions. Both spectra are measured at 9 K with light incident along the [010] direction: many of the structures observed for the light electric field $\mathcal{E}$ parallel to the [001] direction (curve *a*) are absent or weaker, if $\mathcal{E}$ is perpendicular to it (curve *b*).

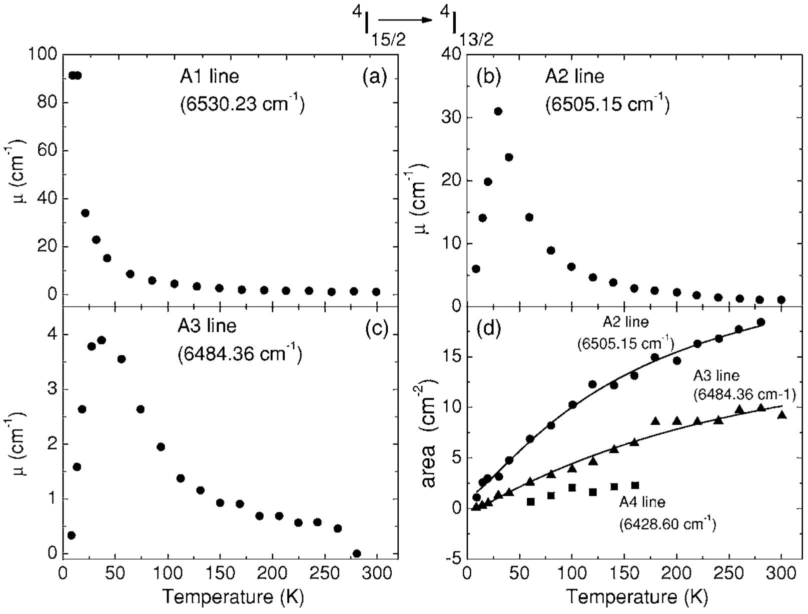

FIG. 7. Temperature dependence of the amplitude and area of a few Ai lines within the $^4I_{15/2} \rightarrow {^4I_{13/2}}$ Er^{3+} transition for a BaY_2F_8:Er^{3+} 2 at. % sample (res. = 0.1 cm^{-1}). Panels (a), (b), and (c) display the amplitude vs. temperature T for the A1 (6530.23 cm^{-1}), the A2 (6505.15 cm^{-1}), and the A3 (6484.36 cm^{-1}) lines, respectively. Panel (d) displays the area under a given line as a function of the temperature for A2 (circles), A3 (triangles), and A4 (6428.60 cm^{-1}, squares) lines, respectively. The continuous lines are drawn as guides for the eye.

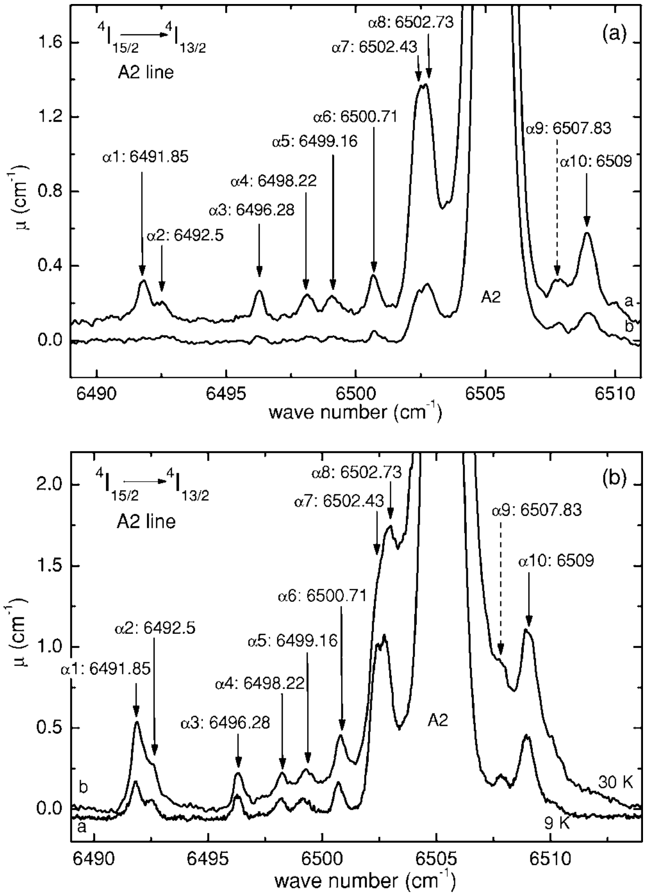

FIG. 8. Dependence of the optical absorption spectra on the light polarization and on the temperature for the analysis of the additional lines accompanying the A2 line (6505.15 cm^{-1}) within the $^4I_{15/2} \rightarrow {}^4I_{13/2}$ transition. Spectra measured at 9 K on BaY_2F_8:Er^{3+} 20 at. % samples. Panel (a) displays two polarized spectra with the light beam propagating along the [010] direction (res. = 0.1 cm^{-1}): curve *a*—light electric field $\mathcal{E}$ parallel to the [001] direction; curve *b*—$\mathcal{E}$ perpendicular to the [001] direction. Panel (b) displays the spectra at 9 K (curve *a*, res. = 0.04 cm^{-1}) and at 30 K (curve *b*, res. = 0.1 cm^{-1}).

With the aim of evaluating the Judd-Ofelt parameters, spectra were also recorded at 180 and 300 K by using unpolarized light incident along three different orthogonal directions (see Sec. IV B). Anisotropy effects were detected as well, although they were not as pronounced as those displayed in Fig. 8(a), due to the line broadening and overlapping occurring at 180 and 300 K. A modest anisotropy was also reported for spectra of Er^{3+}-doped BaY_2F_8 measured at RT in the wave number ranges of the $^4I_{15/2} \rightarrow {}^4I_{11/2}$ and $^4I_{15/2} \rightarrow {}^4I_{9/2}$ transitions.[13]

IV. DISCUSSION

A. Line attribution

Because of the electrostatic and spin-orbit interaction, the $4f^{11}$ configuration of the free Er^{3+} ion is split into 41 manifolds.[17] A further splitting is induced by the crystal field, if the ion is embedded into a crystal lattice. In the case of monoclinic BaY_2F_8, the low symmetry of the crystal field causes the splitting of each $^{2S+1}L_J$ manifold into $(2J+1)/2$ sublevels (Kramers doublets).[17] For example, the ground state $^4I_{15/2}$ should be split into eight sublevels and the first excited state $^4I_{13/2}$ into seven, respectively: such a large number of sublevels, among which the electronic transitions can occur, explains the complexity of the absorption spectra in the region of the $^4I_{15/2} \rightarrow {}^4I_{13/2}$ transition (see Fig. 1). A careful analysis of the spectra, as a function of temperature, is the key for supplying a correct attribution of the absorption lines and for evaluating the ground and excited manifold splitting induced by the crystal field. An example of such a procedure, applied to the $^4I_{15/2} \rightarrow {}^4I_{13/2}$ transition, is illustrated by Fig. 7. The line at 6530.23 cm^{-1} (labeled as A1) is very strong at 9 K where the lowest sublevel of $^4I_{15/2}$ (labeled as 1) must be populated, and decreases monotonically by increasing the temperature [see Fig. 7(a)]. On the contrary, the areas subtended to the lines at 6505.15 cm^{-1} (labeled as A2), at 6484.36 cm^{-1} (labeled as A3), which are both already detectable at 9 K, and at 6428.60 cm^{-1} (labeled as A4), which is absent at 9 K, increase monotonically by increasing the temperature [see Fig. 7(d)], in accordance with the fact that the lowest sublevel population decreases in favor of the sublevels 2, 3, 4,... of the $^4I_{15/2}$ manifold, lying at higher energies. Each line was therefore labeled as Xi, where X=A, B, C,... indicates a given sublevel of an excited manifold and i=1,2,...,8 the sublevel of the ground manifold, from which the absorption transition starts (see Table I, last column). The energy values of sublevels related to the $^4I_{15/2}$, $^4I_{13/2}$, $^4I_{11/2}$, $^4I_{9/2}$, $^4F_{9/2}$, $^4S_{3/2}$, $^2H_{11/2}$, $^4F_{7/2}$, and $^4F_{5/2}$ manifolds were determined and collected in Table I for 9 and 180 K (seventh and eighth columns, respectively). The number of sublevels for each manifold corresponds to the expected value of (2J +1)/2. It should be remarked that the $X1$, $X2$, $X3$, and $X4$ lines could be detected in most of the spectra measured at 9 K and related to the different transitions, therefore the positions of the sublevels 2, 3, and 4 with respect to the position of sublevel 1, which was assumed to lie at energy zero, could be averaged over a large number of data and evaluated with high accuracy. For example the position of the sublevel 2 was estimated from the difference between the wave numbers of 29 pairs of $X1$ and $X2$ lines, spanning over a large spectral range (6500–19 500 cm^{-1}), like that covered by the $^4I_{15/2} \rightarrow {}^4I_{13/2}$, $^4I_{11/2}$, $^4I_{9/2}$, $^4F_{9/2}$, $^4S_{3/2}$, and $^2H_{11/2}$ transitions, respectively. Within the experimental error the values obtained were independent of the spectral range and/or the transition considered. The mean value was estimated as 25.01 ± 0.08 cm^{-1} at 9 K, which should be compared with the value 26 ± 0.5 cm^{-1} at 77 K reported in the literature and obtained from fluorescence measurements performed at a resolution of 0.5 cm^{-1}.[18] The accuracy improvement attained in the present work is related not only to the higher statistics, but also to the better spectral resolution (0.02–0.04 cm^{-1}) and to the measurements performed at lower temperatures. The modest separations $\Delta E_{n,1}$ of the sublevels 2 and 3 with respect to the ground sublevel 1 (i.e., $\Delta E_{2,1}$ and $\Delta E_{3,1} \sim 25$ and 46 cm^{-1}, respectively) explain why the $X2$ and $X3$ lines can be easily detected even at 9 K, being the two sublevels in part populated. In fact, by using the Boltzmann statistics, the

TABLE I. Sublevel positions (cm^{-1}) for different manifolds $^{2S+1}L_J$ of Er^{3+} in BaEr$_2$F$_8$, BaYb$_2$F$_8$, and BaY$_2$F$_8$, as derived from fluorescence and absorption measurements performed at different temperatures. The experimental data are compared to the calculated ones (last but one column). Each sublevel is labeled in the last column with either a number or a letter, see text.

	BaEr$_2$F$_8$	BaYb$_2$F$_8$	BaY$_2$F$_8$						
$^{2S+1}L_J$	77 K[a]	110 K[a]	77 K[b]	77 K[c]	300 K[c]	9 K[d]	180 K[d]	9 K[e]	Sublevel
^{4}I$_{15/2}$	0	0	0	0	0	0.00	0	−4.1	1
	24		26	24	24	25.01	24.2±0.7	26.9	2
	46		47	46	46	45.96	45.6±0.7	44.7	3
	102		103	101	97	101.69	98.5±0.9	104.2	4
	282		284	283	280		280.5±3.9	284.1	5
	330		329	323	330		329.8±4.4	329.4	6
	372		370	365	362		362.0±4.1	372.3	7
	410	410	410	405	400		400.3±1.9	413.6	8
^{4}I$_{13/2}$	6530			6532	6532	6530.23	6530.5	6534.7	A
	6585			6580	6590	6582.44	6581.3	6584.7	B
	6608			6602	6607	6606.23	6605.3	6610.5	C
	6701			6632[f]	6656	6695.60	6698.7	6697.4	D
	6740			6697[g]	6700	6739.10	6737.2	6739.2	E
	6750			6748[h]	6740	6746.19	6745.0	6755.7	F
	6785			6780	6790	6781.45	6779.4	6790.6	G
^{4}I$_{11/2}$	10 232			10 227	10 230	10 227.51	10 227.5	10 215.7	A
	10 275			10 270	10 285	10 270.09	10 269.5	10 260.7	B
	10 313			10 308	10 309	10 307.37	10 306.4	10 301.2	C
	10 328	10 328		10 323	10 325	10 322.43	10 322.2	10 315.6	D
	10 339			10 335	10 335	10 333.19	10 331.9	10 331.5	E
	10 354			10 350	10 348	10 348.88	10 346.6	10 350.5	F
^{4}I$_{9/2}$	12 378			12 385		12 375.79	12 375.6	12 359.4	A
	12 490			12 495		12 486.29	12 484.7	12 483.3	B
	12 580			12 585		12 574.69	12 573.2	12 574.3	C
	12 623			12 627		12 617.80	12 615.5	12 621.5	D
	12 693	12 693		12 695		12 687.63	12 684.9	12 694.5	E
^{4}F$_{9/2}$	15 337	15 336	15312	15 320		15 315.20	15 314.8	15 317.4	A
	15 342		15335	15 340		15 335.51	15 335.0	15 336.1	B
	15 412		15387	15 395		15 389.80	15 388.0	15 391.8	C
	15 447		15420	15 430		15 423.50	15 422.2	15 425.6	D
	15 509		15499	15 507		15 502.50	15 500.0	15 505.7	E
^{4}S$_{3/2}$	18 455	18 453		18 457	18 457	18 449.99	18 449.9	18 439.0	A
	18 522			18 525	18 520	18 518.99	18 516.0	18 505.9	B
^{2}H$_{11/2}$	19 168				19 153[i]	19 168.72	19 169.8	19 177.3	A
	19 200				19 180[j]	19 200.61	19 200.4	19 206.0	B
	19 232				19 210[k]	19 231.50	19 231.5	19 240.5	C
	19 332				19 240	19 328.90	19 327.8	19 307.9	D
	19 352				19 312	19 346.15	19 346.0	19 322.7	E
	19 371				19 373	19 367.02	19 365.4	19 345.8	F
^{4}F$_{7/2}$	20 581					20 580.89	20 581.5		A
	20 603					20 602.41	20 601.6		B
	20 711					20 660.12	20 658.2		C
	20 725					20 722.12	20 719.4		D
^{4}F$_{5/2}$	22 276					22 274.47	22 278.5		A
	22 294					22 292.75	22 291.0		B

TABLE I. (*Continued.*)

	$BaEr_2F_8$	$BaYb_2F_8$	BaY_2F_8						
$^{2S+1}L_J$	77 K[a]	110 K[a]	77 K[b]	77 K[c]	300 K[c]	9 K[d]	180 K[d]	9 K[e]	Sublevel
	22 329					22 327.18	22 324.0		C
$^4F_{3/2}$	22 674								A
	22 691								B
$^2H_{9/2}$	24 545								A
	24 613								B
	24 686								C
	24 742								D
	24 784								E

[a] From Ref. 5.
[b] From Ref. 18.
[c] From Ref. 1.
[d] Present work.
[e] Present work: calculated values, see IV C.
[f] Actually an E4, while E1 is missing.
[g] Actually a D1.
[h] Actually an F1.
[i] Actually a B3.
[j] Actually a C3.
[k] Actually a C2.

ratio of the populations of the sublevels 2 and 3 to that of the sublevel 1 is given by $\exp(-\Delta E_{n,1}/kT)$, i.e., 0.018 and 6.3×10^{-4} for $n=2$ and 3, respectively.

The comparison of the sublevel energy values listed in the seventh and eighth columns of Table I and related to two different temperatures (9 and 180 K, respectively) shows that the sublevel positions and the manifold splittings are affected by the temperature. Such a result is not unexpected because a temperature enhancement induces some lattice expansion, not necessarily isotropic, which can slightly change the crystal field experienced by Er^{3+}. The detailed analysis of the temperature dependence of the line position and width in terms of electron-phonon coupling will be analyzed in a separate paper.

In Table I the energy values of the sublevels are compared with those reported in the literature and related either to two Er^{3+}-doped matrices (BaY_2F_8[1,18] and $BaYb_2F_8$[5]) and to $BaEr_2F_8$, where Er^{3+} substitutes completely Y^{3+}.[5] These experimental data, mainly obtained by means of fluorescence measurements, usually at temperatures higher than those of the present work and with a wave number accuracy in the 0.5–2 cm^{-1} range, show a rather good overall agreement. Examples of a more accurate line attribution, resulting from the present work, with respect to that supplied by the literature, are provided by the lines peaking at 6632, 6697, and 6748 cm^{-1} (at 77 K, see the fifth column in Table I): these were previously identified as D1, E1, and F1 lines, respectively (within the $^4I_{15/2}\rightarrow{}^4I_{13/2}$ transition), but they are actually E4, D1, and F1, respectively.[1] Such an incorrect attribution is easily justified due to the large number of overlapping lines, exhibited by spectra measured at 77 K, as in the case of Ref. 1. Still more difficult was the correct attribution of the lines peaking at 6656, 6700, 6740, 19 153, 19 180, and 19 210 cm^{-1}, respectively, listed in the sixth column of Table I, since the spectra measured at 300 K show broad and overlapped bands.

As already noticed in Ref. 5, there is no large difference among the energy levels of Er^{3+} in BaY_2F_8, $BaYb_2F_8$, and $BaEr_2F_8$ (see Table I), although differences in the oscillator strength are recorded between BaY_2F_8 and $BaYb_2F_8$ from one side and $BaEr_2F_8$ on the other. Such a difference can be easily accounted for by comparing the Judd-Ofelt parameters related to the three systems (see Sec. IV B and Table III).

B. Judd-Ofelt parameters

Transitions between $4f$ states are forbidden in the electric dipole approximation for free rare earth atoms and ions. Whenever they are embedded in a solid, the crystal field makes the transitions partially allowed. A Judd-Ofelt analysis[20,21] was carried out for the absorption spectra recorded at 180 K. The line strengths $S(aJ,bJ')\equiv S_{\mathrm{exp}}$ were experimentally determined by the TPM method,[25] and the Judd-Ofelt parameters Ω_t ($t=2$, 4, 6) were determined by minimizing the rms deviation δ between S_{exp} and

$$S(aJ,bJ') \equiv S_{\mathrm{th}} = \sum_{t=2,4,6} \Omega_t |\langle aJ|U^{(t)}|bJ'\rangle|^2, \qquad (1)$$

using the squared reduced matrix elements for the Er^{3+} ion tabulated in Ref. 32, after subtracting the calculated magnetic dipole contribution (which was found to be significant only for the $^4I_{15/2}\rightarrow{}^4I_{13/2}$ transition) to S_{exp}.

The values of $S_{\mathrm{exp}}^{(i)}$ obtained for each transition considered are listed in Table II together with the values of $\bar{\sigma}$ (manifold barycenter wave number) and of the refractive index n (which was calculated by the Sellmeier dispersion equation with literature parameters[33] for BaY_2F_8 and was found to be in excellent agreement with values measured at wave num-

TABLE II. Values of $\bar{\sigma}$ (at 180 K), n, S_{exp} (from spectra measured at 180 K), and S_{th} for different transitions. S_{exp} and S_{th} are given in units of 10^{-20} cm^2.

Transition	$\bar{\sigma}$(cm^{-1})	n	S_{exp}	S_{th}[a]	S_{th}[b]	S_{th}[c]
$^4I_{15/2}\rightarrow{}^4I_{13/2}$	6617	1.517	2.21 2.66[d]	2.03	2.13	2.21
$^4I_{15/2}\rightarrow{}^4I_{11/2}$	10 303	1.519	0.47	0.58	0.60	0.63
$^4I_{15/2}\rightarrow{}^4F_{9/2}$	15 372	1.523	0.93	0.89	0.95	0.93
$^4I_{15/2}\rightarrow{}^4S_{3/2}$	18 513	1.526	0.19	0.30	0.31	0.33
$^4I_{15/2}\rightarrow{}^2H_{11/2}$	19 234	1.527	1.35	1.35	1.35	1.35
$^4I_{15/2}\rightarrow{}^4F_{7/2}$	20 560	1.529	0.63	0.92	0.97	1.00
$^4I_{15/2}\rightarrow{}^4F_{5/2}$	22 274	1.531	0.20	0.30	0.32	0.33

[a] All the transitions listed are considered for the δ minimization.

[b] All the transitions listed are considered, except the $^4I_{15/2}\rightarrow{}^4F_{7/2}$, for the δ minimization.

[c] The three strongest transitions ($^4I_{15/2}\rightarrow{}^4I_{13/2}$, $^4F_{9/2}$, and $^2H_{11/2}$) are considered for the δ minimization.

[d] Includes the magnetic dipole contribution.

bers close to the spectral regions where the Er^{3+} transitions occur[34]). Table II also lists the S_{th} values obtained in three ways: (a) by including in the minimization procedure all the seven transitions listed; (b) by including all the transitions except the $^4I_{15/2}\rightarrow{}^4F_{7/2}$, whose S_{exp} was probably affected by a relatively large uncertainty due to baseline subtraction problems; and (c) by including only the three strongest transitions ($^4I_{15/2}\rightarrow{}^4I_{13/2}$, $^4I_{15/2}\rightarrow{}^4F_{9/2}$, and $^4I_{15/2}\rightarrow{}^2H_{11/2}$, which contribute for 75% of the whole absorption strength). In the latter case one has three equations, which can be exactly solved with respect to the three J-O parameters. The so-obtained Judd-Ofelt parameters, displayed in Table III, are quite stable, and no dramatic worsening in the agreement between S_{exp} and S_{th} is found for the excluded transitions (Table II).

The present J-O parameters are compared in Table III to those reported in the literature for BaY_2F_8 and $BaEr_2F_8$.[35,36] The values of Ω_2, Ω_4, and Ω_6, listed in columns 2–6 are comparable, although those resulting from the present analysis are slightly higher. The difference may arise from the fact that the parameters quoted in the literature (fifth column) are attributed to BaY_2F_8:Er,[35] but the experimental data, taken from Ref. 5 and used to compute them, seem to be related rather to a $BaYb_2F_8$:Er^{3+} sample. This hypothesis is supported by the similarity of these parameters (fifth column) with those listed for $BaYb_2F_8$ (sixth column).[5] The slight differences between the two data sets might arise from the different transitions used in the minimization procedure.

A more relevant difference occurs between the J-O parameters for Er^{3+} as a dopant in BaY_2F_8 and $BaYb_2F_8$ (second to sixth column) and for Er^{3+} as a matrix component in $BaEr_2F_8$ (seventh column).[38]

The spontaneous emission probability

$$A = S(aJ,bJ')\frac{64\pi^4 e^2\bar{\sigma}^3}{3h(2J+1)}\frac{n(n^2+2)^2}{9}, \tag{2}$$

and the radiative decay time

$$\tau_{r,\mathrm{JO}} = \frac{1}{\sum_{bJ'} A_{aJ,bJ'}} \tag{3}$$

for several transitions were also calculated by using the J-O parameters listed in Table III, third column (six transitions are considered for their evaluation, see above). In Table IV the values of A and $\tau_{r,\mathrm{JO}}$ are listed and the latter are com-

TABLE III. Judd Ofelt parameters Ω_n and δ (given in units of 10^{-20} cm^2) obtained from the present data and compared to those quoted in the literature as related to the BaY_2F_8:Er^{3+} system. The data related to $BaYb_2F_8$ and $BaEr_2F_8$ are also displayed.

Parameter	BaY_2F_8[a]	BaY_2F_8[b]	BaY_2F_8[c]	BaY_2F_8 (?)[d]	$BaYb_2F_8$[e]	$BaEr_2F_8$[f]
Ω_2	1.44	1.39	1.44	1.06	1.08	0.43
Ω_4	0.48	0.54	0.45	0.4	0.38	1.21
Ω_6	1.36	1.42	1.49	0.91	0.98	1.1
δ	0.20	0.13	…			

[a] Present work: all the transitions listed in Table II are considered.

[b] Present work: all the transitions listed in Table II are considered, except the $^4I_{15/2}\rightarrow{}^4F_{7/2}$.

[c] Present work: only the three strongest transitions among those listed in Table II are considered.

[d] From Ref. 35: very likely the system is $BaYb_2F_8$ rather than BaY_2F_8, see text.

[e] From Ref. 5.

[f] From Ref. 36.

TABLE IV. Spontaneous emission coefficient A, radiative lifetime $\tau_{r,\mathrm{JO}}$, as obtained from the present analysis on a $\mathrm{BaY_2F_8{:}Er^{3+}}$ 2 at. % sample, and radiative lifetime $\tau_{r,m}$, measured in the present work and by different authors. The values of $\tau_{r,\mathrm{JO}}$ and $\tau_{r,m}$ are given in ms. The $F_{\mathrm{Er}}^{\mathrm{at}}$ is also indicated (in parentheses). The manifold of the initial level is given, while the final one is $^4\mathrm{I}_{15/2}$ for all the transitions considered. A_{Tk} is the spontaneous emission coefficient as obtained from the J-O analysis according to Ref. 36.

Initial level	$A(\mathrm{s}^{-1})$	$\tau_{r,JO}(2\%)$	$\tau_{r,m}(0.5\%)$	$\tau_{r,m}(1\%)$	$\tau_{r,m}(2\%)$	$\tau_{r,m}(5\%)$	$\tau_{r,m}(10\%)$	$\tau_{r,m}(20\%)$	$\tau_{r,m}(50\%)$	$\tau_{r,m}(100\%)$	$A_{Tk}(\mathrm{s}^{-1})$
$^4\mathrm{I}_{13/2}$	98.6	10.1	10.8[a]			10.6[b,c]		8.3[d]			80.5
	119.6[e]	8.4[e]									116[e]
			15.0±3[f]		16.0±2[f]						
$^4\mathrm{I}_{11/2}$	139.0	7.2	11.0[a]				11.0[c,g]	6.7[d]			104
			9.9[f]		10.0[f]		9.6[b,c]	10.1[h]			
$^4\mathrm{I}_{9/2}$	476.6	2.1		0.0096[b]		0.0096[b]	0.0096[b]	0.0082[b]	0.0042[b]	0.00024[b]	115
$^4\mathrm{F}_{9/2}$	868	1.2	0.3[a]				0.43[c,g]				1085
			1.06[f]		0.91[f]		0.67[c,i]				
			1.08[c]				0.4[b,c]				
$^4\mathrm{S}_{3/2}$	1663.8	0.60	0.83[d]	0.60[g]			0.035[g]				1369
			0.61[a]	0.63[b]		0.075[b]	0.03[b]	0.0087[i]	0.0005[i]	<0.0002[b]	
			0.59[h]	0.73[c,i]				0.009[h]			
			0.696[f]		0.57[f]						
$^2\mathrm{H}_{9/2}$	2212.2	0.45						0.025[d]			

[a] From Ref. 36, $T_{\mathrm{meas}}=300$ K.
[b] From Ref. 13, $T_{\mathrm{meas}}=300$ K.
[c] According to the quoted authors, $\tau_{r,m}$ does not depend on $F_{\mathrm{Er}}^{\mathrm{at}}$.
[d] From Ref. 19, $T_{\mathrm{meas}}=77$ K.
[e] Includes the magnetic dipole contribution.
[f] Present work, $T_{\mathrm{meas}}=180$ K.
[g] From Ref. 1, $T_{\mathrm{meas}}=300$ K.
[h] From Ref. 37, $T_{\mathrm{meas}}=300$ K.
[i] From Ref. 1, $T_{\mathrm{meas}}=77$ K.

pared with the radiative lifetimes $\tau_{r,m}$ measured at different temperatures and for different $\mathrm{F}_{\mathrm{Er}}^{\mathrm{at}}$, either in the present work or quoted in the literature.[1,13,19,36] This also allowed a more straightforward comparison with $\mathrm{BaY_2F_8{:}Er^{3+}}$ literature data, since Ref. 36 does not supply the J-O parameters, but rather the spontaneous emission coefficients A_{Tk}, which are listed in Table IV and compared to those evaluated in the present work according to Eq. (3). The overall agreement is reasonably good, if $\tau_{r,\mathrm{JO}}$ and $\tau_{r,m}$ are compared for comparable $\mathrm{F}_{\mathrm{Er}}^{\mathrm{at}}$. In this framework large difference is observed between $\tau_{r,\mathrm{JO}}$ and $\tau_{r,m}$ for the $^4\mathrm{I}_{9/2}$ level: however this result can be accounted for by the interpretation already given for their very short $\tau_{r,m}$ by Knowles and Jenssen, according to whom the $^4\mathrm{I}_{9/2}$ population quickly relaxes to the metastable $^4\mathrm{I}_{11/2}$ level by strong nonradiative decay.[13] The good agreement between $\tau_{r,\mathrm{JO}}$ and $\tau_{r,m}$ for the $^4\mathrm{S}_{3/2}$ level confirms the correctness of our choice for the J-O parameter determination, notwithstanding the non-negligible difference between S_{th} and S_{exp} for the weak $^4\mathrm{I}_{15/2}\rightarrow{}^4\mathrm{S}_{3/2}$ transition (see Table II). The discrepancy between our $\tau_{r,\mathrm{JO}}$ and $\tau_{r,m}$ for the $^2\mathrm{H}_{9/2}$ level might arise from concentration induced quenching, since the unique available $\tau_{r,m}$ value is related to a highly Er-doped sample ($\mathrm{F}_{\mathrm{Er}}^{\mathrm{at}}=20\%$). In principle the sum in Eq. (3) should be evaluated on all the transitions connecting the single crystal field sublevels belonging to the rare earth manifolds. The spontaneous emission coefficients can be obtained from the absorption data through the Einstein relations. From an experimental point of view this approach is practically impossible, for different reasons. In 9 K spectra the main lines are often out of scale, therefore the subtended area cannot be measured; moreover the absorption lines related to transitions starting from the more excited sublevels of the ground manifold cannot be monitored: they become detectable for example at 180 K (see Table I) where, on the other hand, a remarkable overlapping among the absorption lines forbids the correct evaluation of the area subtended to most of them.

C. Crystal-field and Newman's superposition model

From the theoretical point of view, a calculation of the energy levels of the $4f^N$ configurations in solids based on the single-ion model usually yields good results, being also important to understand the microscopic origin of the crystal-field (CF) potential at the RE^{3+} site. The RE^{3+} Hamiltonian can be written as

$$\hat{H}=\hat{H}_{\mathrm{FI}}+\hat{H}_{\mathrm{CF}}, \tag{4}$$

where $\hat{H}_{\mathrm{FI}}$ is the free-ion part of the total Hamiltonian $\hat{H}$, while $\hat{H}_{\mathrm{CF}}$ describes the CF interaction. The atomic part of Eq. (4) is written as

$$\hat{H}_{\mathrm{FI}} = E_{av} + \sum_k F^k \hat{f}_k + \zeta \hat{H}_{SO} + \alpha \hat{L}(\hat{L}+1) + \beta \hat{G}(G_2) + \gamma \hat{G}(R_7) + \sum_i T^i \hat{t}_i + \sum_j M^j \hat{m}_j + \sum_k P^k \hat{p}_k, \tag{5}$$

where $k=2, 4, 6$; $i=2, 3, 4, 6, 7, 8$; $j=0, 2, 4$; the reader can refer to the literature for a detailed description of the various operators and parameters, which have become quite standard.[39] The CF Hamiltonian is written as

$$\hat{H}_{\mathrm{CF}} = \sum_k \sum_q B_k^q \hat{C}_k^q, \tag{6}$$

where the tensor operators $\hat{C}_k^q$ are expressed according to Wybourne normalization.[40] The energy levels experimentally measured at 9 K (seventh column in Table I) were fitted with the above theoretical model;[41] the agreement between experimental and calculated energy levels given in the last but one column in Table I is quite good, with a rms deviation of 6.3 cm^{-1}.

The resulting CF parameters were analyzed by means of Newman's superposition model,[23] which states that the CF potential experienced by the rare earth ion is the sum of axially symmetric individual contributions from each ligand. In this framework, the CF parameters which appear in H_{CF} can be expressed as

$$B_k^q = \sum_\ell \bar{B}_k(R_\ell) K_k^q(\theta_\ell, \varphi_\ell), \tag{7}$$

where K_k^q are the coordination factors defined in Ref. 23 and R_ℓ is the distance between the RE ion and the ℓth ligand. Assuming the power law

$$\bar{B}_k(R_\ell) = \bar{B}_k(R_0)\left(\frac{R_0}{R_\ell}\right)^{t_k}, \tag{8}$$

where the "standard ligand distance" R_0 was fixed at 2.275 Å (i.e., the average Y^{3+}-F^- distance[4]), the values of the intrinsic parameters were fitted so that the CF parameters obtained from the experimental data can be correctly reproduced by Eq. (7). It is known that, when a paramagnetic ion is substituted into a diamagnetic host, local distortions of the surrounding sites may take place. In this case, the parameters calculated within Newman's superposition model do not match those obtained by the experimental data fit without taking into account an anisotropic compression[41] (about 2% in size) of the F^- ligand cage surrounding the Er^{3+} site. The intrinsic parameters were determined as: $\bar{B}_2(R_0) \simeq 1020\ \mathrm{cm}^{-1}$; $\bar{B}_4(R_0) \simeq 490\ \mathrm{cm}^{-1}$; $\bar{B}_6(R_0) \simeq 290\ \mathrm{cm}^{-1}$, with $t_2=5$; $t_4=6$; $t_6=10$. On the other hand, the large uncertainties displayed by some of the fitting parameters (Table V) were put in relation with a possible off-center position of the Er^{3+} ion with respect to the original Y^{3+} position. The results of our calculations[41] are in line with an absolute deviation $\Delta \leqslant 0.05$ Å in both directions along the C_2 symmetry axis.

TABLE V. Comparison between the crystal-field parameters (cm^{-1}) obtained from the experimental data fitting and those calculated by applying Newman's superposition model. In the latter case, the uncertainties are estimated taking into account a possible off-center position for the Er^{3+} ion (Ref. 41).

Parameter	Data fit	Superposition model
B_2^0	−450±30	−450±20
B_2^2	60±50	60±40
B_4^0	−1430±130	−1330±90
B_4^1	350±270	430±150
B_4^2	110±100	220±130
B_4^3	5±120	−100±130
B_4^4	410±80	400±40
B_6^0	470±170	550±90
B_6^1	−250±180	−270±70
B_6^2	−50±75	−20±50
B_6^3	−80±120	−10±30
B_6^4	390±80	340±10
B_6^5	−370±60	−310±50
B_6^6	250±90	30±20

D. Concentration effects

1. General remarks

The experimental results (Sec. III A and Figs. 1–5) show that, by increasing the Er^{3+} concentration, the line amplitude (Figs. 1 and 2 and Figs. 4 and 5) and width (Fig. 3) increase and new, weak lines appear (Figs. 2, 4, and 5, where the new lines are indicated by arrows). Henceforward the new lines are referred as the additional lines. The increase of all the line amplitudes with the Er^{3+} concentration is expected and is a direct proof that the lines, of negligible amplitude in the nominally pure sample (Sec. III A and curves *a* in Figs. 1 and 4), are induced by Er^{3+}. For the lowest $\mathrm{F}_{\mathrm{Er}}^{\mathrm{at}}$ (i.e., 0.5 and 2 at. %) a proportionality between the line amplitude and $\mathrm{F}_{\mathrm{Er}}^{\mathrm{at}}$ can be caught at a glance, by comparing curves *b* and *c* in Fig. 1, in fact curve *b*, which displays the spectrum of a $\mathrm{BaY_2F_8{:}Er^{3+}}$ 0.5 at. % sample magnified by a factor four, exhibits practically the same line amplitudes as curve *c*, related to a $\mathrm{BaY_2F_8{:}Er^{3+}}$ 2 at. % sample. For higher $\mathrm{F}_{\mathrm{Er}}^{\mathrm{at}}$ it is more difficult to verify the general trend between the line amplitude and $\mathrm{F}_{\mathrm{Er}}^{\mathrm{at}}$ because the main lines ($X1$ lines) are very strong and, thus, either out of scale or affected by the detector nonlinearity. By assuming a linear dependence between the line amplitude and the $\mathrm{F}_{\mathrm{Er}}^{\mathrm{at}}$ at very low Er^{3+} concentration, it was possible to estimate very roughly the Er^{3+} doping as ~50 p.p.m. in the nominally pure sample (Fig. 4).

2. Line width

As a general remark, the line width is rather small for lines occurring at low wave numbers; compare, for example, in Fig. 1, the widths of the lines peaking below 6650 cm^{-1} with those appearing at higher wave numbers. The effect becomes more pronounced for lines monitoring transitions to higher energy lying levels. For example in a $\mathrm{BaY_2F_8{:}Er^{3+}}$ 2

TABLE VI. Absorption coefficient μ, half-maximum full width W, and ratio $\mathcal{Q} \equiv \mu \times W / N_{\mathrm{Er}}$ at 9 K for the A3 and B3 lines ($^4\mathrm{I}_{15/2} \rightarrow {}^4\mathrm{I}_{13/2}$ transition), peaking at 6484.36 and 6536.48 cm^{-1}, respectively, as a function of $\mathrm{F}_{\mathrm{Er}}^{\mathrm{at}}$ and of the Er^{3+} concentration N_{Er}.

$\mathrm{F}_{\mathrm{Er}}^{\mathrm{at}}$ %a. f.	$N_{\mathrm{Er}} \times 10^{-20}$ (cm^{-3})	μ_{A3}(cm^{-1})	W_{A3}(cm^{-1})	$\mathcal{Q}_{A3} \times 10^{18}$ (cm)	μ_{B3}(cm^{-1})	W_{B3}(cm^{-1})	$\mathcal{Q}_{B3} \times 10^{18}$(cm)
0.5	0.64	0.07	0.108	1.2	0.04	0.2	1.25
2	2.57	0.13	0.18	0.91	0.34	0.17	2.25
12	15.4	0.57	0.42	1.6	0.84	0.46	2.51
20	25.7	1.92	1.41	10.5	7.26	0.91	26.5

at. % sample the width of the A2 lines peaking at 6505.16 ($^4\mathrm{I}_{15/2} \rightarrow {}^4\mathrm{I}_{13/2}$), 10 202.27 ($^4\mathrm{I}_{15/2} \rightarrow {}^4\mathrm{I}_{11/2}$), and 19 143.63 cm^{-1} ($^4\mathrm{I}_{15/2} \rightarrow {}^2\mathrm{H}_{11/2}$) is 0.1, 0.53, and 1.6 cm^{-1}, respectively. Such a broadening can be in part accounted for by considering that for high lying levels the spontaneous emission decay channels are many more than for the low ones. This involves a shortening of the radiative lifetimes τ_{aJ}, as confirmed by Table IV, and, as a consequence, a line broadening. A shortening of the radiative lifetime by increasing the starting level energy is reported also for $\mathrm{BaYF}_5:\mathrm{Er}^{3+}$ crystals.[12]

However, the main source of line broadening is the inhomogeneous one, being caused by the presence of Ba, Y, F, and Er isotopes, by the $^{167}\mathrm{Er}^{3+}$-related hyperfine splitting, by the disorder due to defects and to Er^{3+} random distribution. A remarkable broadening occurs for a given line by increasing the Er^{3+} concentration, as demonstrated by Fig. 3, where curves *a*, *b*, and *c* portray the A3 lines at 6484.36 cm^{-1} in $\mathrm{BaY}_2\mathrm{F}_8$ samples doped with 2, 12, and 20 Er^{3+} at. %, respectively. The peak amplitudes are normalized to one to emphasize the effect. Table VI lists the half-maximum full width W of two absorption lines peaking at 6484.36 (A3) and 6536.48 cm^{-1} (B3), respectively, for all the concentrations investigated: the line at 6484.36 cm^{-1} broadens by a factor 27 by increasing $\mathrm{F}_{\mathrm{Er}}^{\mathrm{at}}$ from 0.5% to 20%. In the nominally pure sample the Er^{3+} lines are narrower, for example the width of the A1 line (at 6530.23 cm^{-1}) might be even less than 0.02 cm^{-1} in comparison with the value of 0.13 cm^{-1} for the same line in the $\mathrm{BaY}_2\mathrm{F}_8:\mathrm{Er}^{3+}$ 0.5 at. % sample. The result is in agreement with that reported for 1 p.p.m. Er^{3+}-doped LiYF_4,[15] for which the linewidth is even narrower (in the range $10^{-3}-4 \times 10^{-3}$ cm^{-1}, see Sec. I). Similar broadening was observed for all the lines, even if this is less pronounced in the case of lines already rather broad in low concentration samples, as for the B3 line peaking at 6536.48 cm^{-1} (see Table VI).

The result can be explained by considering that the random distribution of Er^{3+} ions over the Y^{3+} sites causes lattice disorder, thus a given Er^{3+} ion, notwithstanding it is shielded by the eight F^- polyhedron, experiences slightly different crystal fields, depending on its separation from other Er^{3+} ions. By increasing the concentration, the average distance among the Er^{3+} ions decreases and the Er^{3+}-Er^{3+} interactions are monitored by the inhomogeneous line broadening. In fact, the line shape changes too by increasing the Er^{3+} concentration. In less doped samples the narrowest lines are clearly Lorentzian shaped, as shown for example by Figs. 3 (curve *b* and $\mathrm{F}_{\mathrm{Er}}^{\mathrm{at}}=12\%$) and 6 ($\mathrm{F}_{\mathrm{Er}}^{\mathrm{at}}=0.5\%$). In Fig. 3 the line shape changes from Lorentzian (curve *b*) to Gaussian (curve *c*) by increasing $\mathrm{F}_{\mathrm{Er}}^{\mathrm{at}}$ from 12% to 20%, supporting a concentration induced inhomogeneous line broadening. Similar results and explanation were reported for very narrow lines, as those monitoring the stretching vibration of OH^- in sillenites and in KMgF_3 at 9 K.[28,42] In both cases, the disorder typical of mixed crystals (in sillenites) or induced by other impurities, as Pb^{2+} in KMgF_3, caused line broadening and line shape changes.

As mentioned above, a line broadening suggests a radiative lifetime shortening, due to short range interactions and energy transfer among Er^{3+} ions. A decrease of the radiative lifetime by increasing the Er^{3+} concentration is reported for the $^4\mathrm{I}_{9/2} \rightarrow {}^4\mathrm{I}_{15/2}$ and $^4\mathrm{S}_{3/2} \rightarrow {}^4\mathrm{I}_{15/2}$ transitions at 300 K in $\mathrm{BaY}_2\mathrm{F}_8$ samples[1,13] (see Table IV) and for the $^4\mathrm{I}_{13/2} \rightarrow {}^4\mathrm{I}_{15/2}$, $^4\mathrm{I}_{11/2} \rightarrow {}^4\mathrm{I}_{15/2}$, $^4\mathrm{F}_{9/2} \rightarrow {}^4\mathrm{I}_{15/2}$, and $^4\mathrm{S}_{3/2} \rightarrow {}^4\mathrm{I}_{15/2}$ transitions in BaYF_5 crystals.[12] Furthermore in $\mathrm{BaEr}_2\mathrm{F}_8$, where Y^{3+} ions are completely substituted by Er^{3+}, self-quenching is expected[36] and observed,[13] as shown for the emissions from the $^4\mathrm{I}_{9/2}$ and $^4\mathrm{S}_{3/2}$ manifold, respectively (see the eleventh column in Table IV).

Another important feature to underline is that the area under the A3 line at 6484.36 cm^{-1} vs. $\mathrm{F}_{\mathrm{Er}}^{\mathrm{at}}$ increases more than linearly (Fig. 3). The ratio $\mathcal{Q}$ between the linewidth W times the peak absorption coefficient μ and the Er^{3+} concentration N_{Er} is reported in Table VI, for the A3 and B3 lines, peaking at 6484.36 and 6536.48 cm^{-1}, respectively. The ratio $\mathcal{Q}$ can be assumed roughly constant for both lines, within the experimental error, for $\mathrm{F}_{\mathrm{Er}}^{\mathrm{at}}=0.5\%$, 2%, and 12%, but shows a strong enhancement for $\mathrm{F}_{\mathrm{Er}}^{\mathrm{at}}=20\%$. $\mathcal{Q}$, being by definition proportional to ratio between the area $\mathcal{A}$ (under the considered absorption line) and N_{Er}, should be proportional to the line strength S and should depend on the refraction index n. A change of n with the Er^{3+} concentration might occur. In the absence of a detailed n dependence on the Er^{3+} doping, a rough estimate can be done as follows. The refraction index depends on the electronic polarizability α of atoms/ions composing the material and α is proportional to r^3, being r the atomic/ionic radius. Therefore a large change of the $\mathrm{BaY}_2\mathrm{F}_8$ refraction index is not expected as a consequence of the Er^{3+} substitution for Y^{3+}, since the two ions have practically the same ionic radius (i.e., $\mathrm{r}_{\mathrm{Er}}=1.14$ Å and $\mathrm{r}_{\mathrm{Y}}=1.16$ Å in fluorides with coordination number=8).[22] Anyway, the n dependence on Er^{3+} concentration cannot justify by itself the sharp $\mathcal{Q}$ increase by increasing $\mathrm{F}_{\mathrm{Er}}^{\mathrm{at}}$ from 12% to 20%. More likely, the result can be explained by assuming that the transition probability S is strongly modified by increasing F_{Er}^{at} to 20%. Such a change can be accounted for by the symmetry modification of the crystal field experienced by a given Er^{3+}, if it is surrounded at a rather short distance by other Er^{3+} ions. The local symmetry is lowered with a consequent increase of the oscillator strength. At $F_{Er}^{at}=20\%$, the BaY_2F_8 crystal should be regarded as a mixed BaY_2F_8-$BaEr_2F_8$ crystal rather than an Er^{3+}-doped BaY_2F_8. This result suggests that even the J-O parameters can be affected by the Er^{3+} concentration at high F_{Er}^{at} values, as also reported for YAG crystals.[38]

Usually a superlinear dependence of the area under an absorption line on the related absorption center concentration (in the present case the Er^{3+} ions) suggests that the line is related to a complex center (for example, an aggregate of Er^{3+} ions), but this is not the case for the A3 and B3 lines considered. In fact, such lines are due to transitions from the sublevel 3 of the ground manifold to the A and B sublevels of the excited $^4I_{13/2}$ manifold, respectively (see Sec. IV A): they are originated by the same absorption center that gives rise to the corresponding A1 and B1 lines, peaking at 6530.23 and 6582.44 cm^{-1}, respectively. These lines are present even in the nominally pure BaY_2F_8 sample with weak Er^{3+} traces, i.e., in very dilute solid solution, where the Er^{3+} ions must be assumed as isolated. Moreover, the attribution of the lines to dispersed Er^{3+} is strongly supported by the excellent agreement of the measured line positions, listed in Table I (seventh column), with those calculated on the basis of a theoretical model (ninth column), which assumes that Er^{3+} is isolated in the BaY_2F_8 crystal field (see Sec. IV C).

3. Additional lines

The additional lines, which appear in the spectra of samples doped with the highest F_{Er}^{at} (i.e., 12% and 20%) and are indicated by arrows, for example in Figs. 4 and 5, cannot be explained by the theoretical model based on Er^{3+} dispersed in the BaY_2F_8 matrix. They accompany the strong *Xi* lines associated to isolated Er^{3+}, being much weaker and covering a wave number range of ~20 cm^{-1} around the corresponding *Xi* (mainly on the low wave number side). Figures 4(a) and 4(b) portray those accompanying, within the same $^4I_{15/2} \rightarrow {}^4I_{13/2}$ transition, the A2 and A1 lines peaking at 6505.15 and 6530.23 cm^{-1}, respectively, while Figs. 5(a) and 5(b) show those related to the same kind of line, i.e., the A1, peaking at 15 315.20 and 19 168.72 cm^{-1} within two different transitions, i.e., $^4I_{15/2} \rightarrow {}^4F_{9/2}$ and $^4I_{15/2} \rightarrow {}^2H_{11/2}$, respectively. The association of the additional lines to a given *Xi* line is not based only on the fact that they are close to it, but is also supported by the same line strength behavior as a function of temperature and light polarization, as shown in Fig. 8 for the additional lines accompanying the A2 line ($^4I_{15/2} \rightarrow {}^4I_{13/2}$ transition). In fact, a rotation of the polarized light electric field $\mathcal{E}$ by 90° causes a decrease both of the A2 and of the additional lines: compare curves *a* and *b* in Fig. 8(a), which are related to $\mathcal{E}$ along the [001] direction and orthogonal to it, respectively. Moreover, Fig. 8(b) shows a peak amplitude increase both for the main A2 and for the additional lines, by enhancing the temperature from 9 K (curve *a*) to 30 K (curve *b*). Such a behavior is expected for transitions starting from an excited sublevel of the ground manifold, whose population increases by increasing the temperature [see Sec. IV A and Fig. 7(d)]. On the contrary, the A1 lines and the associated additional lines decrease, as expected for transitions that start from the lowest sublevel of the ground manifold, whose population decreases by increasing the temperature [see Sec. IV A and Fig. 7(a)]. Around each main *Xi* line, a set of additional lines can be envisaged: they are identified by α_n labels. Sequences of up to ten α lines were observed for the low energy lying transitions [see Fig. 4(a)]. By increasing the transition energy, overlapping to main *Xi* lines, line broadening and noise make more difficult the task of distinguishing the single additional lines.

What is the origin of the additional lines? They must be related to the presence of Er^{3+}, because they appear in all the typical wave number ranges of Er^{3+} transitions. They cannot be attributed to hyperfine splitting or isotopic effects, because these should cover a wave number range around a given *Xi* line much smaller, as shown for example in Er^{3+}-doped $LiYF_4$.[15] They cannot be related to the Er^{3+} interaction with unwanted impurity, as OH or other RE^{3+}. In fact, the OH doping of the present samples was found below the detection limit of our apparatus, which is quite sensitive (see Sec. II). The RE^{3+} ions, present as traces in the two samples exhibiting the additional lines, were not the same, i.e., Ho^{3+} and Tm^{3+} were detected in the sample with $F_{Er}^{at}=12\%$ and Nd^{3+} in that with $F_{Er}^{at}=20\%$. As the additional lines, for example the stronger ones indicated by arrows in Figs. 4(b) and in Fig. 5(a), are peaking at the same wave number in the two samples, they cannot be attributed to the interaction of Er^{3+} with different RE^{3+}. A reasonable hypothesis about their origin is that the additional lines are related to an Er^{3+}-Er^{3+} interaction. At a F_{Er}^{at} value as high as 20%, every five Y^{3+} sites, one is occupied by an Er^{3+}, thus more or less loose Er^{3+} pairs (or clusters) may form, in the sense that Er^{3+} substitutes Y^{3+} in two (or more) near neighbor (n.n.) or next near neighbor (n.n.n.) YF_8 polyhedra. Therefore the crystal field experienced by an Er^{3+} ion in such loose clusters is slightly different from that probed by an isolated Er^{3+} and is finely tuned according to the number and position of Er^{3+} in n.n. or n.n.n. YF_8 polyhedra. This might explain the presence of a rather large number (up to ten) of additional lines accompanying a given main *Xi* line originated by an isolated Er^{3+}. A given α_n line should correspond to a given Er^{3+} pair or cluster (α_n center). The wave number covered by an entire set of additional lines is of the order of ~20 cm^{-1}: this means that the energy level tuning for Er^{3+} embedded in pairs or clusters spans over a fraction lower than 0.3%, even for the lowest energy lying transition (i.e., the $^4I_{15/2} \rightarrow {}^4I_{13/2}$ in the 6500–6700 cm^{-1} range). The position of the best resolved and identified additional lines associated to different transitions are collected in Table VII. A given α line within the set, e.g., the α_6, could be associated to the A1 lines belonging to different transitions and, in the case of the $^4I_{15/2} \rightarrow {}^4I_{13/2}$ transition, associated also to the A2, B1, and C1 lines. In the following an α additional line, associated to a given *Xi* line, is defined as a *Xi*-type line and its position in the spectrum is indicated as ν_{Xi}. In Table VII the energy level scheme for a given α_n center is compared to those of an

TABLE VII. Line positions ν_{A1} of the A1-type additional lines for different Er^{3+} centers indicated by α_n for different transitions, separation $\Delta E_{2,1}$ between the first excited (2) and the ground (1) sublevels of the lowest manifold $^4I_{15/2}$, and $\Delta E_{B,A}$ and $\Delta E_{C,A}$ separations between an excited (B or C) and the lowest sublevel (A) of higher energy lying manifold. All the figures are given in cm^{-1} and obtained from spectra measured at 9 K. For comparison the data related to isolated Er^{3+} in the BaY_2F_8 matrix, labeled as $Er^{3+}(1)$ center, and those related to Er^{3+} in $BaEr_2F_8$, labeled as $Er^{3+}(T)$ are reported: the data are taken from Table I, seventh and second columns, respectively.

Transition	Center	ν_{A1}	$\Delta E_{2,1}$	$\Delta E_{B,A}$	$\Delta E_{C,A}$
$^4I_{15/2} \rightarrow {}^4I_{13/2}$	α_3	6515.92	19.64	57.61	71.58
	α_4	6518	19.78	57.63	73.11
	α_5	6519.79	20.63	55.84	71.32
	α_6	6522.19	21.48	54.7	77.72
	$\alpha_{7\text{-}8}$	6527.41	25	51.14	75.44
	α_{10}	6527.6	27.2	48.56	73.7
	$Er^{3+}(1)$	6530.23	25.01	52.21	76.0
	$Er^{3+}(T)$	6530	24	55	78
$^4I_{15/2} \rightarrow {}^4F_{9/2}$	α_3	15293.9		27.89	
	α_4	15293.9		30.3	
	α_5	15297		29.4	
	α_6	15301		28.6	
	$\alpha_{7\text{-}8}$	15311.4		21.1	
	$Er^{3+}(1)$	15315.20	25.07	20.3	74.6
	$Er^{3+}(T)$	15337		5	75
$^4I_{15/2} \rightarrow {}^2H_{11/2}$	α_3	19157			
	α_4	19157.8			
	α_5	19159.3			
	α_6	19160.8			
	$Er^{3+}(1)$	19168.72	25.09	31.89	62.78
	$Er^{3+}(T)$	19168		32	64

isolated Er^{3+} in BaY_2F_8 and of an Er^{3+} in $BaEr_2F_8$, indicated as $Er^{3+}(1)$ and $Er^{3+}(T)$ centers, respectively. For such a purpose, the following energy differences ΔE were evaluated: $\Delta E_{2,1} \equiv \nu_{A1} - \nu_{A2}$, $\Delta E_{B,A} \equiv \nu_{B1} - \nu_{A1}$, and $\Delta E_{C,A} \equiv \nu_{C1} - \nu_{A1}$. As explained in Sec. IV A, $\Delta E_{2,1} \equiv \nu_{A1} - \nu_{A2}$ is the separation between the first excited (2) and the ground (1) sublevel of the lowest manifold $^4I_{15/2}$, $\Delta E_{B,A}$ and $\Delta E_{C,A}$ are the separations between an excited (B or C) and the lowest sublevel (A) of the excited manifold. Each α center is characterized by a given set of ΔE: the values are rather close to each other and to those exhibited by the $Er^{3+}(1)$ and $Er^{3+}(T)$ centers. The result shows the fine tuning of the energy levels around those of the isolated Er^{3+} in the BaY_2F_8 and of Er^{3+} completely surrounded by other Er-F_8 polyhedra as in $BaEr_2F_8$. None of the ΔE sets for the α centers coincides with that of $BaEr_2F_8$: this rules out the possible phase separation of $BaEr_2F_8$ as small precipitates inside BaY_2F_8. Such a conclusion is also supported by the x-ray diffraction measurements performed on BaY_2F_8:Er^{3+} 20 at. %, which excluded the presence of any separated phase (see Sec. II). Therefore even in the highest Er^{3+} concentration sample, Er^{3+} should be found as an isolated ion, responsible for the main *Xi* lines, and as embedded in more or less loose pairs or clusters, monitored by the weak α_n lines. This supports the high Er^{3+} solubility in BaY_2F_8 crystals. As a rule, a fast quenching from high temperature of a sample containing clusters (for example, an alkali halide doped with divalent cations) succeeds in breaking them, with a consequent increase of the simplest defect fraction.[7] Thus a thin sample of BaY_2F_8:Er^{3+} 20 at. % was kept at 600 °C for 4 h and then quenched to room temperature. The quenching does not reduce significantly the additional lines, being unable to break the loose Er^{3+} clusters or pairs due to the high dopant concentration, i.e., from a statistical point of view the average distance among Er^{3+} ions does not change. This is at variance with alkali halides and alkali-earth fluorides, where the clustering process starts at much lower concentration of dopants, which, being aliovalent impurities (e.g., Cd^{2+} in NaCl or Gd^{3+} in CaF_2), require charge compensation (see Sec. I). Therefore the additional lines in BaY_2F_8 do not monitor some kind of tightly bound Er^{3+} dimer (two Er^{3+} ions could not fit in an eight F^- polyhedron), but rather an Er^{3+}-Er^{3+} interaction for relatively short separations of two (or more) ErF_8 polyhedra in BaY_2F_8. Another point in favor of these assumptions lies in numerical calculations based on Newman's superposition model (Sec. IV C); one of the F^--F^- bonds in the ligand cage was supposed to change its length due to the presence of Er^{3+} in one of the neighbor or nearest-neighbor polyhedra, and the resulting variations in the calculated spectra were evaluated as a function of this bond length. Despite the roughness of this model, the general trend reported in Table VII is reproduced, in that the correct order of magnitude for the energy shift from each line, associated to an $Er^{3+}(1)$ center, is found if a reasonable distortion ($\leq 5\%$) is accounted for. In this framework, several additional lines may arise due to the fact that each Er^{3+} ion involved can occupy different off-center positions (Sec. IV C). On this basis, the concentration induced effects can be regarded as due to crystal field modification induced on the surroundings of a given Er^{3+} ion, assumed as a probe, by other Er^{3+} ions more or less close to it.

Other much weaker lines were detected in Er^{3+}-doped BaY_2F_8 samples with $F_{Er}^{at}=0.5\%$, 2%, and 12%, respectively. Such lines cannot be attributed, as the α-lines, to Er^{3+}-Er^{3+} interaction because they are absent in the sample with the highest F_{Er}^{at} (i.e., 20%). On the other hand, as they occur in the typical range of Er^{3+} transitions, they should be tentatively attributed to Er^{3+} perturbed by some unwanted impurity, most likely O^{2-} since the presence of OH^- was excluded due to the lack of its vibrational absorption features (see Sec. II) and oxygen contamination in fluorides can hardly be avoided completely.[43,44] However, this remains a hypothesis which we plan to verify in the future, by studying BaY_2F_8:Er^{3+} samples in which the presence of O^{2-} impurities is intentionally favored.

V. CONCLUSIONS

The complex high resolution absorption spectra of BaY_2F_8 single crystals doped with various amounts of Er^{3+}, measured over a wide wave number (500–24 000 cm^{-1}) and temperature (9–300 K) ranges, have been analyzed in detail, also taking advantage of theoretical calculations and radiative lifetime measurements. The results provide a thorough description and a deep insight on the spectroscopic characteristics induced by isolated and interacting Er^{3+} ions in a system that is relevant for laser applications. The main conclusions can be summarized as follows.

(1) The isolated Er^{3+} transitions from the fundamental $^4I_{15/2}$ to the excited $^4I_{13/2}$, $^4I_{11/2}$, $^4I_{9/2}$, $^4F_{9/2}$, $^4S_{3/2}$, $^2H_{11/2}$, $^4F_{7/2}$, $^4F_{5/2}$, and $^4F_{3/2}$ manifolds are identified. The crystal field induced splitting is evaluated with high accuracy for all manifolds (e.g., the separation between the two first sublevels of the ground manifold is estimated as 25.01 ± 0.08 cm^{-1} against the 26 ± 0.5 cm^{-1} value quoted in the literature). The complete energy scheme is supplied, providing the correct absorption line attribution.

(2) The experimentally determined energy levels are successfully fitted with a single-ion model and the crystal field parameters are obtained. The parameter analysis by means of Newman's superposition model suggests a distortion of the F^- polyhedron around Er^{3+} ions and a possible off-center position of the dopant ions with respect to the original Y^{3+} position.

(3) The Judd-Ofelt parameters are evaluated with good accuracy by applying the TPM procedure and compared to those quoted in the literature for similar systems as $BaYb_2F_8:Er^{3+}$ and $BaEr_2F_8$. The correction due to the magnetic dipole contribution for the $^4I_{15/2}\rightarrow{}^4I_{13/2}$ transition is calculated. From the J-O parameters the radiative lifetimes are estimated for a few manifolds ($^4I_{13/2}$, $^4I_{11/2}$, $^4I_{9/2}$, $^4F_{9/2}$, $^4S_{3/2}$, and $^2H_{9/2}$) and compared with the experimental values obtained in the present work and/or quoted in the literature for different Er^{3+} concentrations. The overall agreement is quite satisfactory.

(4) The inhomogeneous broadening of the lines (as narrow as 0.13 cm^{-1} in samples with $F_{Er}^{at}=0.5\%$) and the oscillator strength enhancement, induced by increasing the Er^{3+} concentration, demonstrates how the crystal field transitions of the isolated Er^{3+} are sensitive probes of the disorder caused by a random distribution of other Er^{3+} ions.

(5) The weak additional lines appearing in samples with the highest Er^{3+} concentrations (i.e., 12% and 20%) prove the presence of more or less loose Er^{3+} clusters. For some of them an energy level scheme is provided that coincides neither with that of isolated Er^{3+} nor of $BaEr_2F_8$.

ACKNOWLEDGMENTS

The authors wish to thank C. Mora and M. Curti of IMEM-CNR (Parma) for their technical help, Dr. M. Cornelli, Dr. A. Losi, Dr. A. Ruffini, and Dr. A. Sperzagni for some FT spectra measurements, Professor A. Pietraszko and Dr. J. Damm of INTIBS (Wrocław, Poland) for x-ray diffraction measurements, and Professor H.P. Jenssen of CREOL (Orlando, Florida, USA) for supplying some samples.

---

*Electronic address: rosanna.capelletti@unipr.it

[1] A. A. Kaminskii, S. E. Sarkisov, F. Below, and H.-J. Eichler, Opt. Quantum Electron. **22**, S95 (1990).

[2] A. A. Kaminskii, Phys. Status Solidi A **148**, 9 (1995).

[3] M. Pollnau, W. Lüthy, H. P. Weber, T. Jensen, G. Huber, A. Cassanho, H. P. Jenssen, and R. A. McFarlane, Opt. Lett. **21**, 48 (1996).

[4] L. H. Guilbert, J. Y. Gesland, A. Bulou, and R. Retoux, Mater. Res. Bull. **28**, 923 (1993).

[5] A. A. Kaminskii, B. P. Sobolev, S. E. Sarkisov, G. A. Denisenko, V. V. Raybchenkov, V. A. Fedorov, and T. V. Uvarova, Izv. Akad. Nauk SSSR, Neorg. Mater. **18**, 482 (1982).

[6] I. N. Kurkin, K. P. Chernov, and Yu. K. Chirkin, Sov. Phys. Solid State **21**, 549 (1979).

[7] R. Capelletti, Radiat. Eff. **74**, 119 (1983) and references therein.

[8] J. Corish, C. R. A. Catlow, P. W. M. Jacobs, and S. H. Ong, Phys. Rev. B **25**, 6425 (1982).

[9] D. R. Tallant, D. S. Moore, and J. C. Wright, J. Chem. Phys. **67**, 2897 (1977).

[10] V. Dierolf and M. Koerdt, Phys. Rev. B **61**, 8043 (2000).

[11] H. Eichler, J. Findeisen, B. Liu, A. A. Kaminski, A. V. Butachin, and P. Pauser, IEEE J. Sel. Top. Quantum Electron. **3**, 90 (1997).

[12] L. F. Johnson, H. J. Guggenheim, T. C. Rich, and F. W. Ostermayer, J. Appl. Phys. **43**, 1125 (1972).

[13] D. Knowles and H. P. Jenssen, IEEE J. Quantum Electron. **28**, 1197 (1992).

[14] K. M. Devyatkova, O. N. Ivanova, V. V. Mikhailn, S. P. Chernov, and T. V. Uvarova, Sov. Phys. Dokl. **34**, 443 (1989).

[15] R. M. Macfarlane, A. Cassanho, and R. S. Meltzer, Phys. Rev. Lett. **69**, 542 (1992).

[16] A. Baraldi, R. Capelletti, M. Cornelli, A. Ponzoni, A. Ruffini, A. Sperzagni, and M. Tonelli, Radiat. Eff. Defects Solids **155**, 349 (2001).

[17] G. H. Dieke, *Spectra and Energy Levels of Rare Earth Ions in Crystals* (Wiley & Sons, New York, 1968), p. 46.

[18] L. F. Johnson and H. J. Guggenheim, Appl. Phys. Lett. **19**, 44 (1971).

[19] L. F. Johnson and H. J. Guggenheim, Appl. Phys. Lett. **20**, 474 (1972).

[20] B. R. Judd, Phys. Rev. **127**, 750 (1962).

[21] G. S. Ofelt, J. Chem. Phys. **37**, 511 (1962).

[22] A. A. Kaminskii, *Laser Crystals*, 2nd ed. (Springer-Verlag, Berlin, 1990).

[23] D. J. Newman and B. Ng, *Crystal Field Handbook* (Cambridge University Press, Cambridge, 2000).

[24] A. Toncelli, M. Tonelli, A. Cassanho, and H. P. Jenssen, J. Lumin. **82**, 291 (1999).

[25] L. Zundu, C. Xueyuan, and Z. Tingjie, Opt. Commun. **134**, 415 (1997).

[26] M. F. Joubert, B. Jacquier, C. Linarés, and R. M. Macfarlane, J. Lumin. **47**, 269 (1991).

[27] R. Capelletti, P. Beneventi, E. Colombi, and S. Prato, Nuovo Cimento Soc. Ital. Fis., D **20D**, 859 (1998).

[28] A. Baraldi, P. Bertoli, R. Capelletti, A. Ruffini, and A. Scacco, Phys. Rev. B **63** 134302 (2001).

[29] M. Stavola, L. Isganitis, and M. G. Sceats, J. Chem. Phys. **74**, 4228 (1981).

[30] G. Blasse, Int. Rev. Phys. Chem. **11**, 71 (1992).

[31] F. Cornacchia, L. Palatella, A. Toncelli, M. Tonelli, A. Baraldi, R. Capelletti, E. Cavalli, K. Shimamura, and T. Fukuda, J. Phys. Chem. Solids **63**, 197 (2002).

[32] A. A. Kaminskii, V. S. Mironov, A. Kornienko, S. N. Bagaev, G. Boulon, A. Brener, and B. Di Bartolo, Phys. Status Solidi A **151**, 231 (1995).

[33] R. D. Shannon, R. C. Shannon, O. Medenbach, and R. X. Fischer, J. Phys. Chem. Ref. Data **31**, 931 (2002).

[34] H. P. Jenssen (private communication).

[35] A. A. Kaminskii, V. S. Mironov, and S. N. Bagaev, Phys. Status Solidi A **148**, K107 (1995).

[36] A. M. Tkachuk, S. I. Klokishner, A. V. Poletimova, and M. V. Petrov, Opt. Spektrosk. **60**, 745 (1986).

[37] L. Palatella, A. Di Lieto, P. Minguzzi, A. Toncelli, and M. Tonelli, J. Opt. Soc. Am. B **18**, 1711 (2001).

[38] Q. Y. Wang, S. Y. Zhang, and Y. Q. Jia, J. Alloys Compd. **202**, 1 (1993).

[39] H. M. Crosswhite and H. Crosswhite, J. Opt. Soc. Am. B **1**, 246 (1984).

[40] B. G. Wybourne, *Spectroscopic Properties of Rare Earths* (Interscience, New York, 1965).

[41] N. Magnani, G. Amoretti, A. Baraldi, and R. Capelletti, Eur. Phys. J. B **29**, 79 (2002).

[42] P. Beneventi, R. Capelletti, L. Kovács, Á. Péter, A. M. Lanfredi Manotti, and F. Ugozzoli, J. Phys.: Condens. Matter **6**, 6329 (1994).

[43] R. S. Eachus, R. H. D. Nuttall, M. T. Olm, W. G. McDugle, F. K. Koschnick, Th. Hangleiter, and J.-M. Spaeth, Phys. Rev. B **52**, 3941 (1995).

[44] B. P. Sobolev, Crystallogr. Rep. **47**, S63 (2002).